



DANMARKS TEKNISKE UNIVERSITET

Filtered backprojection imaging

22485 MEDICAL IMAGING SYSTEMS

January 19, 2023



Alvaro Carrera Cardeli
s172254



Federico Medea
s193612

Instructor: Jørgen Arendt Jensen

Contents

1	Introduction	2
2	Methods	2
2.1	Computed tomography	2
2.2	Parallel ray reconstruction	3
2.3	Filtration	4
3	Simulated data	6
3.1	Error analysis	7
3.2	Filtration	8
3.3	Analysis of the parameters of the system	11
3.3.1	Number of detectors	11
3.3.2	Number of projections	12
3.4	Effect of a missing detector	14
4	In-vivo data	16
4.1	Reconstruction analysis	16
4.2	Effect of a missing detector	17
5	Conclusion	18

1 Introduction

Projection radiography and computed tomography are two imaging modalities that are based on the transmission of ionizing radiation through the body. Ionizing radiation is the radiation capable of ejecting electrons from atoms [1]. Tissues and other body structures attenuate the intensity of the beam of ionizing radiation when it passes through them.

Projection radiography is the most common method of medical imaging that uses x-rays [2]. It is used to get images of structures within the body, especially bones. X-ray computed tomography (CT) is another popular imaging modality and it reconstructs cross sections of the body rather than imaging projections [1]. CT is also able to remove the artifacts of overlaying structures that dominate radiographs. However, it produces images with lower resolution than radiographs and requires a higher x-ray dose to the patient.

In this report the filtered backprojection algorithm is implemented in order to reconstruct medical images. The method uses the parallel beam projection geometry and it can manage data from a 180° scan with various number of projections. In order to test and validate the algorithm, it is used the Shepp-Logan phantom that is a standard test image created by Larry Shepp and Benjamin F. Logan in 1974 [3]. A previous filtration in the frequency domain is necessary to enhance image resolution and is made by implementing three different filters: Shepp-Logan filter, Hanning weighted filter and Ram-Lak filter (also known as ramp filter). Thus, a comparison between these filters is carried out to show the different results and define the final system. After that, the method is tested on a clinical image taken from a female patient using a Toshiba scanner at Rigshospitalet. Lastly, the image reconstruction algorithm is tested by simulating the effect of a missing detector in the CT scanner.

2 Methods

In this part of the report, a generic overview of computed tomography is given in Section 2.1. Then the parallel beam mode is described on details in Section 2.2. Lastly, the filtration in frequency domain is introduced in Section 2.3 explaining how the filters were designed and the final aim of filtering the image.

2.1 Computed tomography

When a patient is introduced into a CT scanner, a combination of multiple x-ray measurements are taken from different angles to reconstruct cross-sectional images of the body [1]. Its operations is based on a narrow beam of x-rays that is aimed at a patient

and quickly rotated around the body to form the cross-sectional images. Since exposure takes place at different angles, each two-dimensional projection of the 3-D body contains different information and each horizontal line gives a 1-D projection of a 2-D axial cross-section of the body at that angle. The transformation that takes 1-D projection of a 2-D object over many angles is called the 2-D Radon transform [1]. Therefore by using its mathematical inverse (inverse 2-D Radon transform) it is possible to reconstruct the axial cross section, given a collection of projections.

In order to obtain a projection in a CT system, the x-ray tube generates a short burst of x-rays that propagate through a cross section of the patient. The receivers detect the exit beam intensity integrated along a line between the x-ray source and each detector. The gantry of a CT system holds the x-ray tube and detectors, so that they can remain parallel while being rotated around the patient [1].

The linear attenuation coefficient μ between x-ray tube and detectors measures the quantity of how much the x-ray intensity is reduced by a material. However, different CT scanners have different x-ray tubes and hence different effective energies. So the same object would produce different values of μ on different scanners. In order to compare data from different scanners, the CT number (named h) is calculated from normalizing the measured linear attenuation coefficient at each pixel. It is defined as follows,

$$h = \frac{\mu - \mu_{water}}{\mu_{water}} * 1000 \quad (1)$$

and it is measured in Hounsfield units (HU). Since attenuation values are normalized relative to water, then h equals 0 for water. As regards air, there is no attenuation ($\mu = 0$), thus $h = -1000 HU$, whereas the highest CT number in body is for bone with a value that is typically around 1000 HU.

2.2 Parallel ray reconstruction

Parallel ray reconstruction is one of the algorithms that is possible to use in order reconstruct an image out of the attenuation obtained over the entire cross-section. Parallel ray projections means that a collection of line integrals for parallel lines is taken into account. Firstly, it is important to describe briefly the parallel-ray geometry where x and y are the rectilinear coordinates that represent the patient coordinate system, whereas x' and y' are the CT coordinate system. 2-D Radon transform may be used in order to represent the gantry coordinate system that keeps rotating during scanning. Thus, the 2-D Radon transform of the object that needs to be reconstructed, $f(x, y)$, can be finally expressed

as:

$$p(x', \phi) = \int_{-\infty}^{+\infty} f(x' \cos \phi - y' \sin \phi, x' \sin \phi + y' \cos \phi) dy' \quad (2)$$

where x' is the detector position and ϕ is the gantry rotation. Therefore, $p(x', \phi)$ is called projection for a fixed ϕ , while it is called the 2-D Radon transform of $f(x, y)$ for all angles. A sinogram is the visual representation of the Radon transform of $f(x, y)$ and it is the data that is necessary to reconstruct the image.

Filtered backprojection uses three basic steps to reconstruct an image from a sinogram: filtering, backprojection and summation [1] and this algorithm needs to be performed for all projections. As regards filtration, this first step will be covered more into details in Section 2.3, nevertheless, it is important to mention now that a Fourier transform of projected data is carried out to apply the filter in frequency domain. Before second and third step it is necessary to return in time domain by using the Inverse Fourier Transform (IFT). Thus, backprojection is applied to each filtered projection and eventually a summation with the previous backprojection image is accomplished. Filtered backprojection can be easily summarized by the following equation:

$$\hat{f}(x, y) = \int_0^\pi \int_{-\infty}^{+\infty} |\rho| P(\rho, \phi) e^{j2\pi\rho x'} d\rho d\phi \quad (3)$$

where $\hat{f}(x, y)$ is the reconstructed image, $|\rho|$ is the filter in frequency and $P(\rho, \phi)$ is the projection in the frequency domain. Lastly, the main integral goes from 0 to π applying the inverse Radon transform, since 180° it is the range of action of the system.

2.3 Filtration

Filters have different applications in signal processing systems. The most common use is to reduce/remove the noise, when it is known the signal expected, by applying high-pass, low-pass or band-pass filter to the recovered information. However, there is not signal information in the case of backprojection reconstruction, therefore, it is not possible to apply a filter trying to remove the noise, since it is not known if either the frequencies contain information or noise.

On the other hand, the purpose of this system is to differentiate structures within a blind area, and two structures are distinguished when there is a substantial change between them. In the case of the system, this substantial change is presented as different levels of attenuation over the incisive wave emitted from the transmitters. Therefore, the objective is to detect these sharp changes in attenuation in order to differentiate the structures. This information is contained in the high frequencies of the signals recovered (in this case the projections), thus the filter designed will focus on enhancing this range of frequencies.

Since the filtering is done in the frequency, the transfer functions of the different filters considered are shown in this domain (see figure 1). However, the transfer function of the ideal filter (figure 1, in blue) could be easily converted into the time domain by noticing that a triangle is the convolution of two squares, thus, by knowing the relation,

$$\Pi\left(\frac{t}{T}\right) \xrightarrow{FT} T * \text{sinc}(fT) \quad (4)$$

it is straightforward to conclude that the transfer function of the filter in time domain will have sinc to the square shape. In the case of the other two filters, it is just needed to convolve the transfer function in time with the IFT of the window that weights the transfer function in frequency domain.

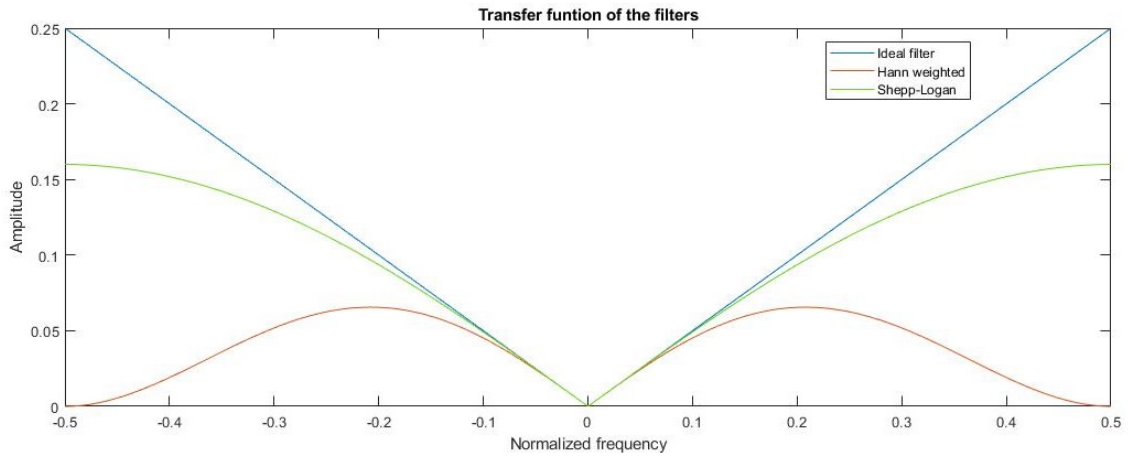


Figure 1: Transfer functions of the filters implemented: Ideal filter (blue), Hann weighted filter (red) and Shepp-Logan filter (green).

Figure 1 shows the ideal filter for this system (in blue), also known as ramp filter. It is important to notice that this filter increases more and more the power of the frequencies as long as the frequencies are getting bigger (thus it enhances high frequencies and reduces low frequencies in relative power). Nevertheless, the main drawback of this filter is that it is also enhancing the noise in the same proportion, thus, in the case of a noisy system, the reconstruction would be in risk to be spoiled by the noise. To control this problem, it was designed the Hann weighted filter (in red) that is the ramp filter multiplied by a Hanning window. This helps to control the enhancement of undesired signal in exchange of reduction in the accuracy of sharp changes detection. Lastly, a third filter was designed, Shepp-Logan filter (in green), that ranges all the possible filters between the ideal and the Hann weighted filters, as the equation 5 states. In the tests run, the filter used was $k = 0.16$.

$$Shepp - Logan_{filter}(i) = Ramp_{filter}(i) * \frac{\sin(\frac{Ramp_{filter}(i)}{k})}{\frac{Ramp_{filter}(i)}{k}} \quad (5)$$

In the following sections the three filters will be tested, in order to choose the one that fits the best in the final system. To conclude, it is important to mention, that the filtration in frequency is applied by multiplying the filter and the spectrum of the signal.

3 Simulated data

The filtered backprojection system was developed from scratch with the software *Matlab R2020a* (see the code in Appendices). In order to test its perform and analyze the parameters that fit better with the system (i.e. filter used, number of projections and number of detectors), it was used the ideal Shepp-Logan phantom.

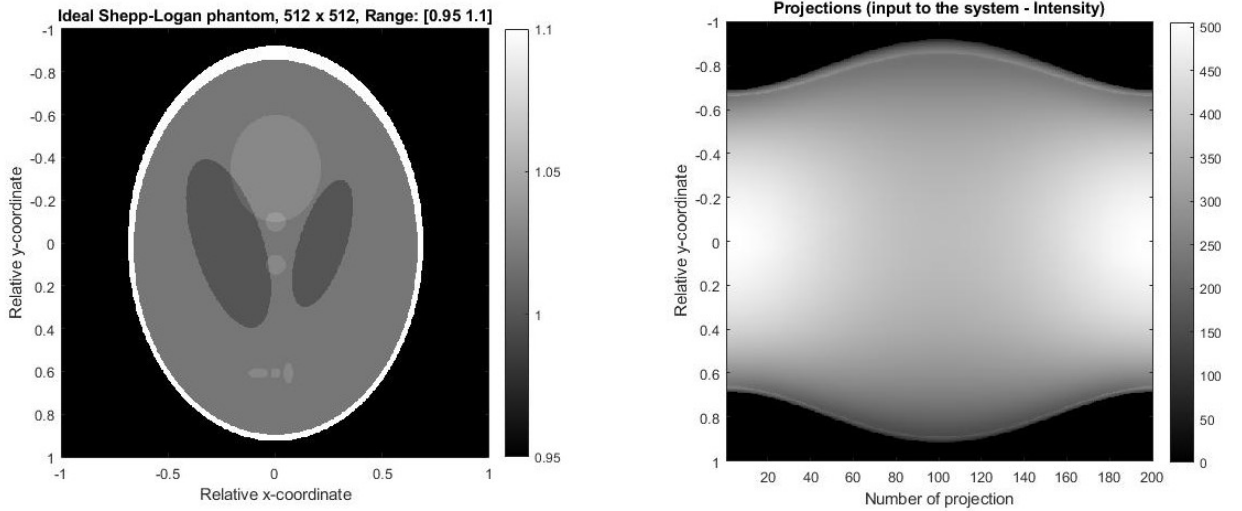


Figure 2: Model used to test the system. (left) Ideal Shepp-Logan phantom. (right) 100 projections of the phantom.

Figure 2 (left) shows the model used, where the main values, that are allocated in the central oval shape, range from 0.95 to 1.1 [HU] of attenuation. Moreover, the right plot shows 100 projections of the ideal Shepp-Logan phantom measured around 180 degrees (i.e. the Radon transform of the phantom for 100 projections). To test the system, the projections will be the input to the system and, the ideal and expected output should be the phantom.

3.1 Error analysis

An error measurement is created to validate the performance of the system. Figure 3 (left) presents the 256 x 256 pixels reconstructed image from 100 projections. The error of this reconstruction is calculated by subtracting point by point the phantom with the obtained image,

$$Error = \sum |(Img_{phantom} - Img_{reconstructed})| \quad (6)$$

leading to figure 3 (center). It can be visually appreciated that a greater contribution of the error comes from the area that has no information in the saturation range considered, therefore, it has been decided to apply a mask leaving only the area of interest and eliminating the contribution of error that differs the evaluation of the performance.

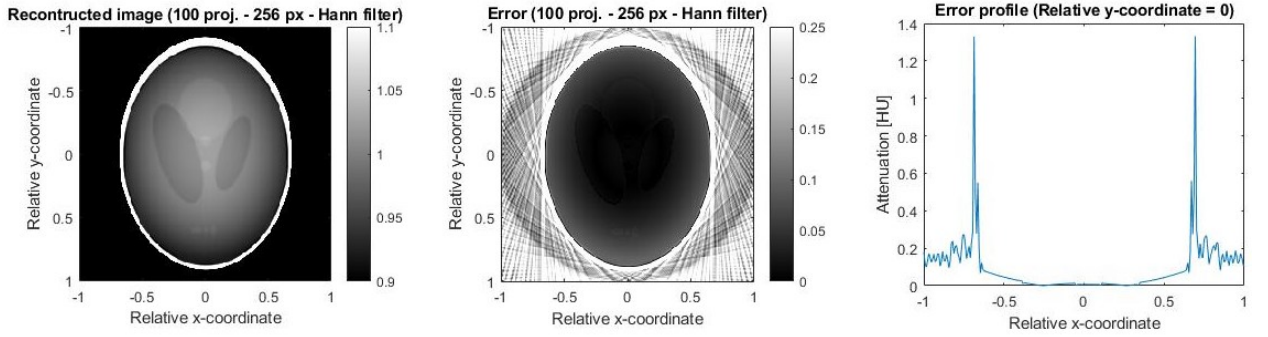


Figure 3: (left) Image of 256 x 256 pixels reconstructed form 100 projections. (center) Error of the reconstruction. (right) Error profile for relative y-coordinate equals to 0.

Figure 4 (left) and (center) shows the mask generated and applied to the reconstruction, respectively. As a result of this mask, in figure 4 (right) can be seen the new profile of the error in contrast with the error profile of figure 3 (right).

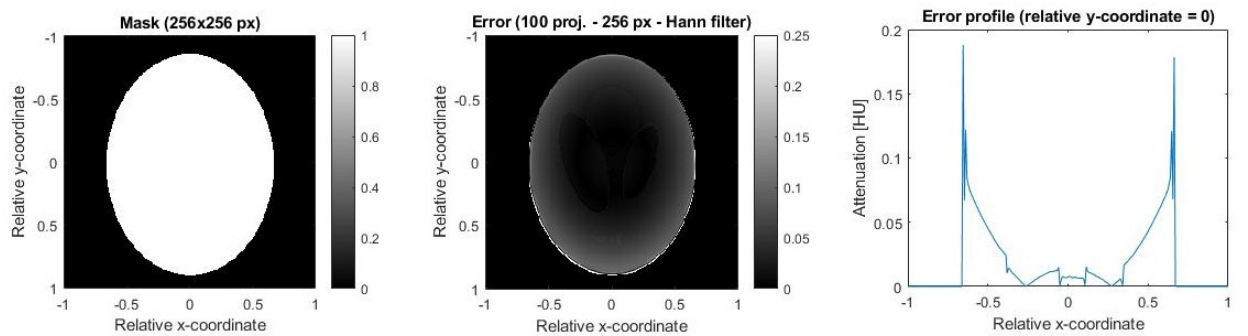


Figure 4: (left) Mask generated. (center) Error of the reconstruction after applying the mask. (right) Error profile for relative y-coordinate equals to 0.

Lastly, it is important to notice that in both cases, error without and with mask, the

largest contributions per pixel come from the edge of the oval shape, which is where there is the sharpest "jump" from one structure (the white contour of the phantom) to another (the inner part of the contour), see figure 5.

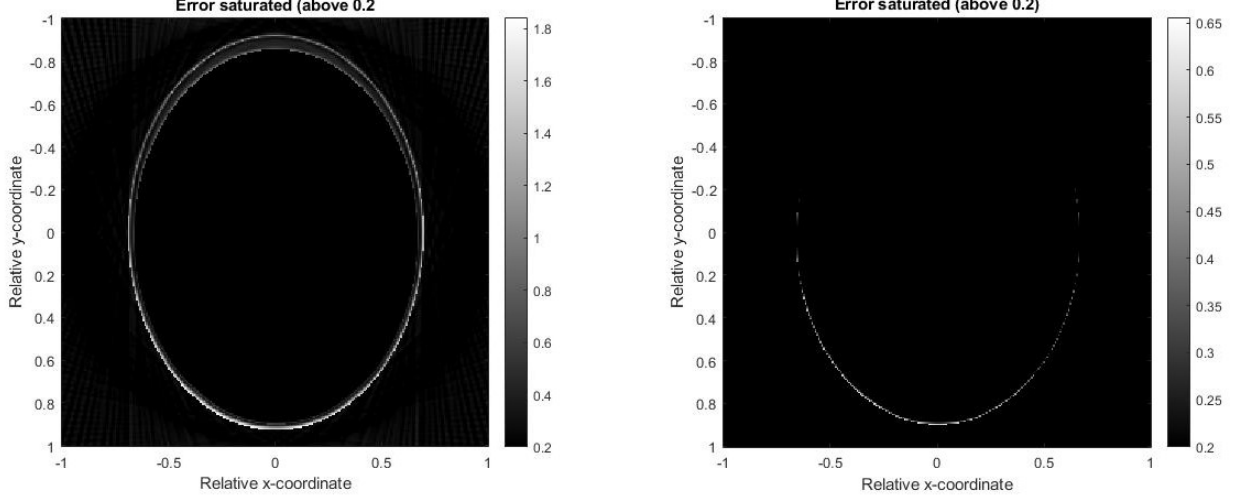


Figure 5: Major contributions to general error. (left) Error of reconstructed image without mask. (right) Error of reconstructed image with mask.

From now on in the report, the error will be studied applying the mask and normalizing by the number of pixels considered in the mask, so it can be expressed as:

$$Error = \frac{\sum(|(Img_{phantom} - Img_{reconstructed})| \cdot Mask)}{\sum Mask} \quad (7)$$

3.2 Filtration

As explained in section 2.3, high frequencies are the ones that help to distinguish structures. So, in the case that the system performs the reconstruction without a filter enhancing high frequencies, it would be impossible to differentiate any structure within the phantom reconstructed (see figure 6, left). Moreover, and as expected, the error obtained is a lot bigger than the results obtained after filtration, 0.1034 in this case. Figure 6 (right) shows how almost all the structures within the phantom are part of the error because the system was unable to recognize them.

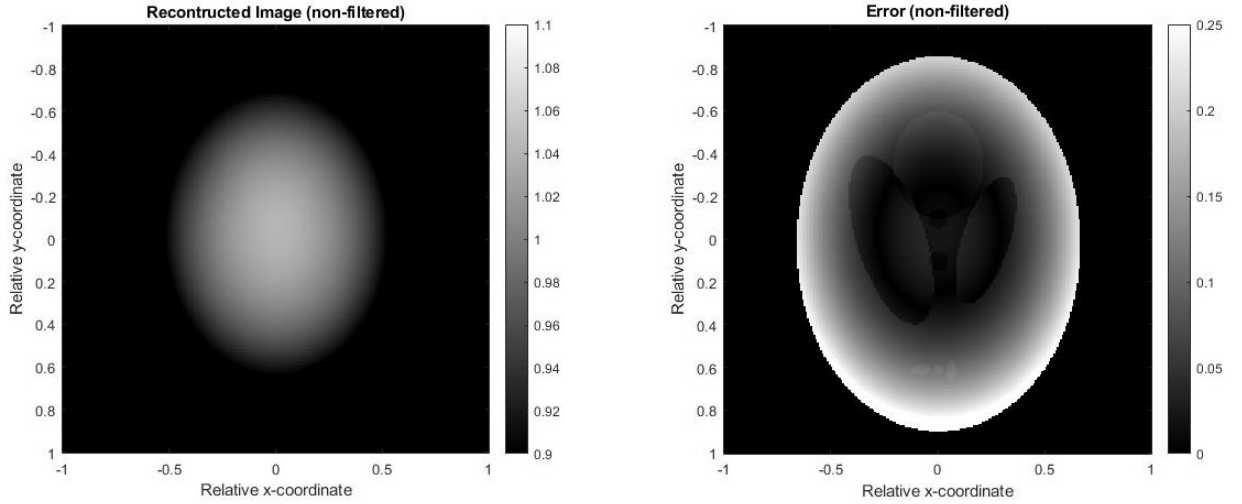


Figure 6: System without filtration. (left) Reconstructed image. (right) Error of the reconstructed image.

Also, in section 2.3 it was introduced the three filters considered and their transfer functions. To understand their behaviors, figure 7 presents the FT of a projection (red) and the FT of the same projection after filtration (green) for the ideal filter, Hann weighted filter and Shepp-Logan filter, from top to bottom, respectively. It is clear that in all the cases high frequencies are enhanced, although with some filters (i.e. Hann weighted filter) this improvement is more controlled than with others (i.e. Ideal filter).

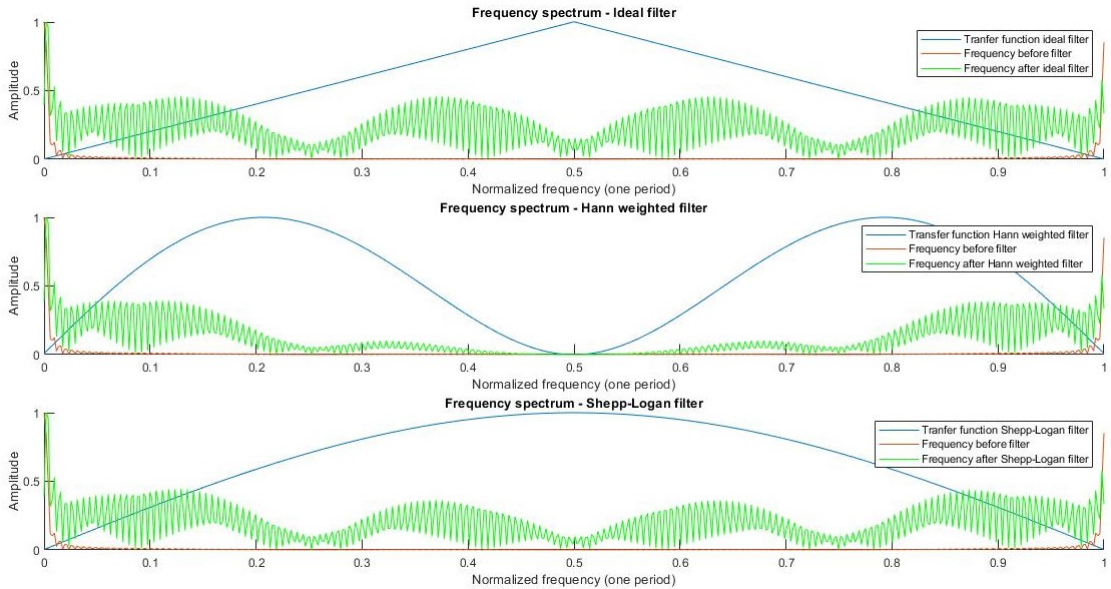


Figure 7: Normalized graphs of transfer function of the filter (blue), frequency of a projection (red) and frequency of the same projection after filtration (green). (top) Ideal filter. (center) Hann weighted filter. (bottom) Shepp-Logan filter.

It is important to notice in figure 7 that for real discrete signals the FT is periodic and symmetric with a periodicity of frequency sampling (f_s). Thus, the normalized frequency at 0.5 represents $f_s/2$ (highest frequency). This means that the range of normalized frequencies of the projection go from 0 to 0.5, so it is easier to notice in the graphs that the high frequencies are being enhanced.

Figure 8 shows the same profile for each of the filters to get a better understanding of the differences between filters in time. The Hann weighted filter (center) has more control over the noise than the ideal filter (left). Whereas, the ideal filter obtains higher peak values at the edges of the structures. This is due to the fact that in this system it is not possible to differ noise from information, thus generating a lower enhancement of the high frequencies prevent from increasing uncontrollable noise in exchange of a lower accuracy in edges detection. Last, Shepp-Logan filter is a balance between the ideal and the Hann weighted filter (right).

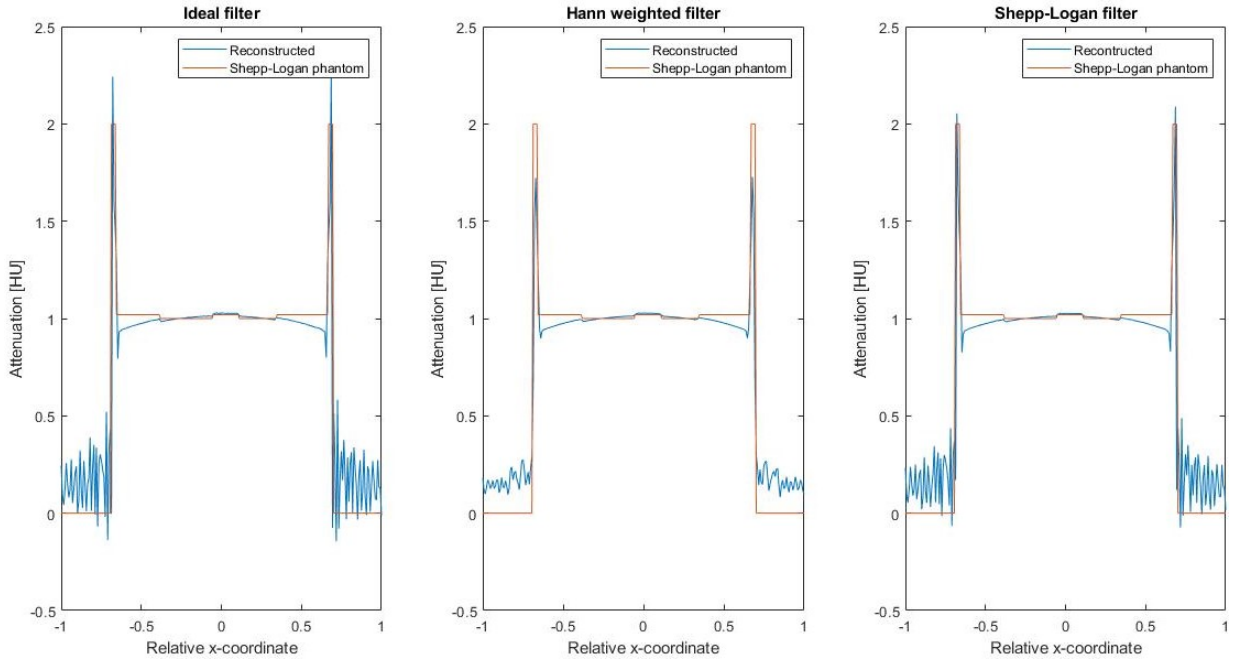


Figure 8: Reconstructed profile (blue) vs. ideal Shepp-Logan phantom profile (red), for a relative y-coordinate equals to 0. (left) Ideal filter. (center) Hann weighted filter. (right) Shepp-Logan filter.

To conclude, in table 1 there are the errors obtained from all the filters with the same input data, and the gain generated by each of the filters. It is important to mention, that the ideal filter has the highest gain, while the Hann weighted filter the lowest, as expected. Moreover, Hann weighted filter has also the lowest error, so it will be the filter used from now on in the results (filter chosen for the design of the system).

	Error	Gain of the filter
Non-filtered	0.1034	-
Ideal filter	0.0475	0.7851
Hann weighted filter	0.0446	0.7838
Shepp-Logan filter	0.0467	0.7848

Table 1: Comparative of the filters' errors (input data: 100 projections and 256 pixels) and gains.

3.3 Analysis of the parameters of the system

The system has two variable parameters that are the number of detectors used to measure a projection and the number of projections measured in 180 degrees. In this section the influence of these parameters in the results will be analysed.

3.3.1 Number of detectors

To test the influence of the number of detectors used, it was generated an input of 64 projections recorded by 128, 256 and 512 detectors. Figure 9 shows the reconstructed images of the three cases going from left to right, from the smallest to the largest number of detectors. At first glance, a slight difference in resolution between images can be seen, due to the pixel size used in each case, but in all cases, all the phantom structures can be easily distinguished, although the three small circles in the bottom of the phantom are clearer with 512 pixels than 128 pixels, due to the resolution of the pixel.

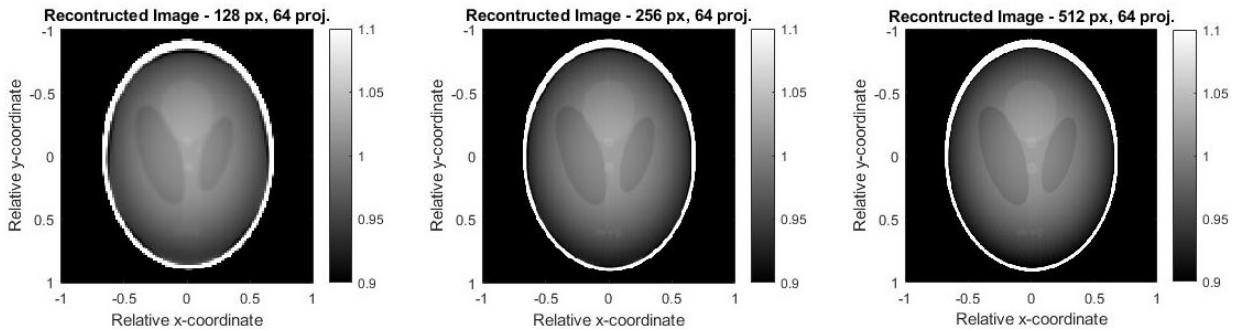


Figure 9: Images reconstructed with 64 projections. (left) 128 x 128. (center) 256 x 256. (right) 512 x 512.

Figure 10 shows that the errors for the three detectors size is similar distributed, concluding that the three are performing similarly. In fact, the errors obtained are almost the same: 0.044, 0.0455 and 0.0447, for 128, 256 and 512 detectors, respectively.

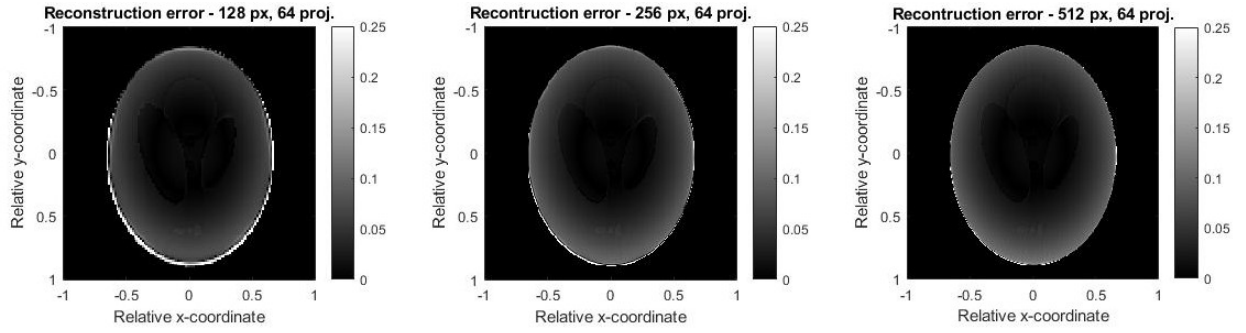


Figure 10: Error of the images reconstructed with 64 projections. (left) 128 x 128. (center) 256 x 256. (right) 512 x 512.

Lastly, it was tested a bit more in detail the influence of this variable by calculating the error generated from using detectors only to the power of two from 2^3 to 2^9 . The result obtained shows the way the error decreases as long as the number of detectors is increased until it is stabilized right below 0.05 with 64 detectors or more (see figure 11).

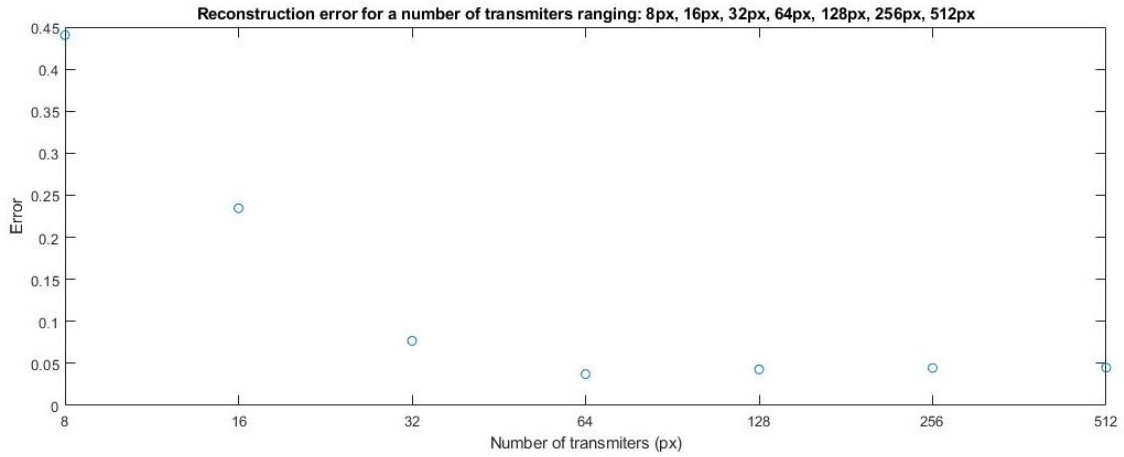


Figure 11: Error trend while increasing the number of detectors.

3.3.2 Number of projections

In this section the influence from number of projections is taken into account in order to see how it affects the image reconstruction. In figure 12 it is showed the reconstruction image of the Shepp-Logan phantom with 22, 64 and 180 projections, from left to right respectively. It is possible to notice how much worse the resolution is for 22 projections (figure 12, left), compared with the other two reconstructions. Indeed, the big circles within the phantom can still be seen, but the small phantom structures on the centre and bottom are not easily recognizable. Moreover, some projections lines are still easily distinguishable on the image, making the appearance of the reconstruction worse. As regards images with 64 and 180 projections (figure 12 center and right, respectively),

they look alike and the level of resolution is high for both of them.

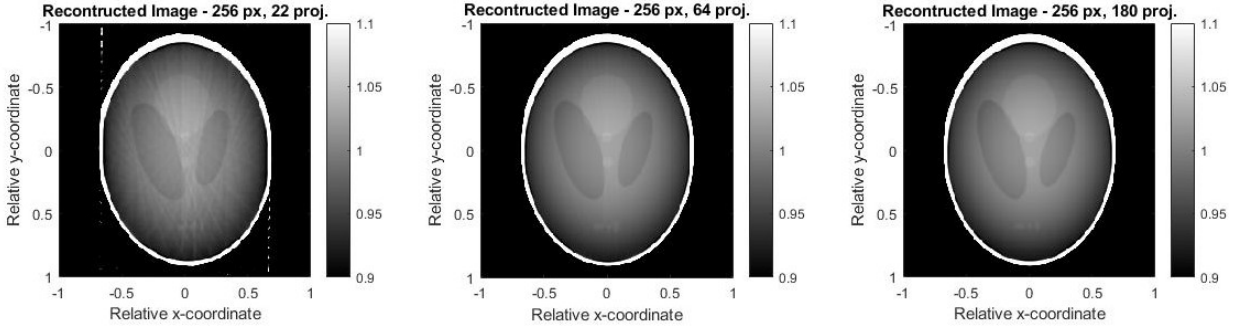


Figure 12: Images reconstructed with 256 pixels. (left) 22 projections. (center) 64 projections. (right) 180 projections.

The error of the three reconstructions is showed in figure 13. It is easy to notice that the center and right error images look almost the same between them (corresponding to 64 and 180 projections, respectively), while in the case of the 22 projections (left) the errors in the edges of the phantom differ from the others due to the fact that the lack of resolution affects more the points that are far from the center of the image. The reconstruction errors are 0.046, 0.0455 and 0.0456 for images with 22, 64 and 180 projections, respectively.

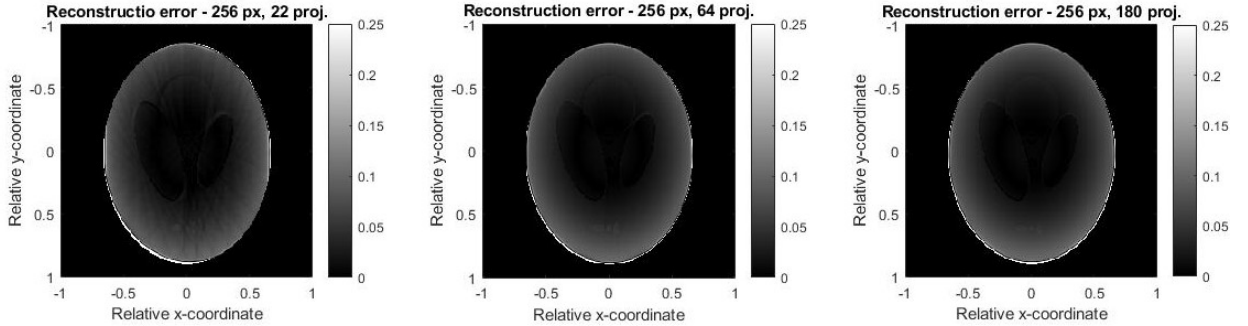


Figure 13: Error of the images reconstructed with 256 pixels. (left) 22 projections. (center) 64 projections. (right) 180 projections.

Lastly, figure 14 compares error obtained from a range of reconstructions with different number of projections. The range of projections considered goes from 3 to 180. It is noticeable an exponential decay of the error as long as the number of projections used is increased, reaching approximately an error of 0.045, where it is stabilized. The minimum number of projections needed to reach this stable error is around 40. However, it is important to notice that the test is run over an ideal phantom with a low range of values in the examined area, therefore it is easier to get lower errors with less projections in this case than in the case that it is used a real phantom. In fact, visually, the reconstruction

of the image improves considerably with more projections, although in both cases the same error is obtained (see figure 12 left vs. center).

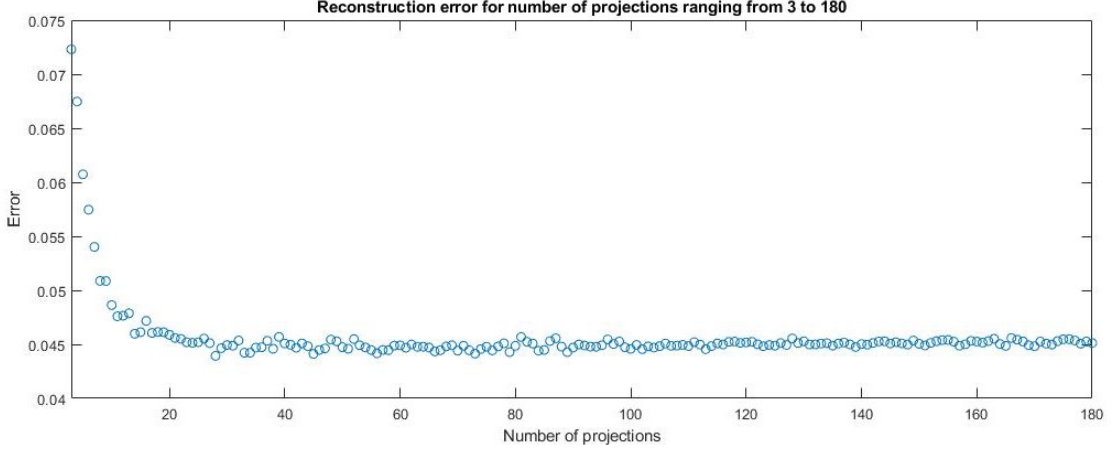


Figure 14: Error trend while increasing the number of projections.

3.4 Effect of a missing detector

There is one last case to be tested that is the inconvenience that would cause when one detector is broken in the system. Since it is important the accuracy of the system for certain diagnoses, the logical procedure would be to either fix the detector or change the system. However, it is proposed an alternative software solution in order to overcome the problem, that it would be interpolating the missing data of the detector broken. Therefore, this data is obtained from the mean between the value recorded by the previous detector and the value recorded by the next detector, as states equation 8.

$$Value_{missing_detector}(i) = \frac{Value_{missing_detector-1}(i) + Value_{missing_detector+1}(i)}{2} \quad (8)$$

Figure 15 (top) shows the reconstructed images when there is a detector failing in the left (detector number 50), center (detector number 128) and right (detector number 206) part of the array of detectors (the array is composed of 256 detectors), respectively plotted from left to right. It is clear the impact caused by the failure of one detector in the reconstructed image, although depending on the location of the detector, the more or less visual information will be recovered. In fact, in the case of central detector failure no visual conclusions can be made out of the reconstructed image (see figure 15, center-top).

In order to overcome this problem, new values are generated to replace the missing values (equation 8). The result obtained for the three cases are shown in figure 15 (bottom), where it can be seen a clear improvement of the reconstructed images and the error

obtained in all the cases is equal to 0.0446.

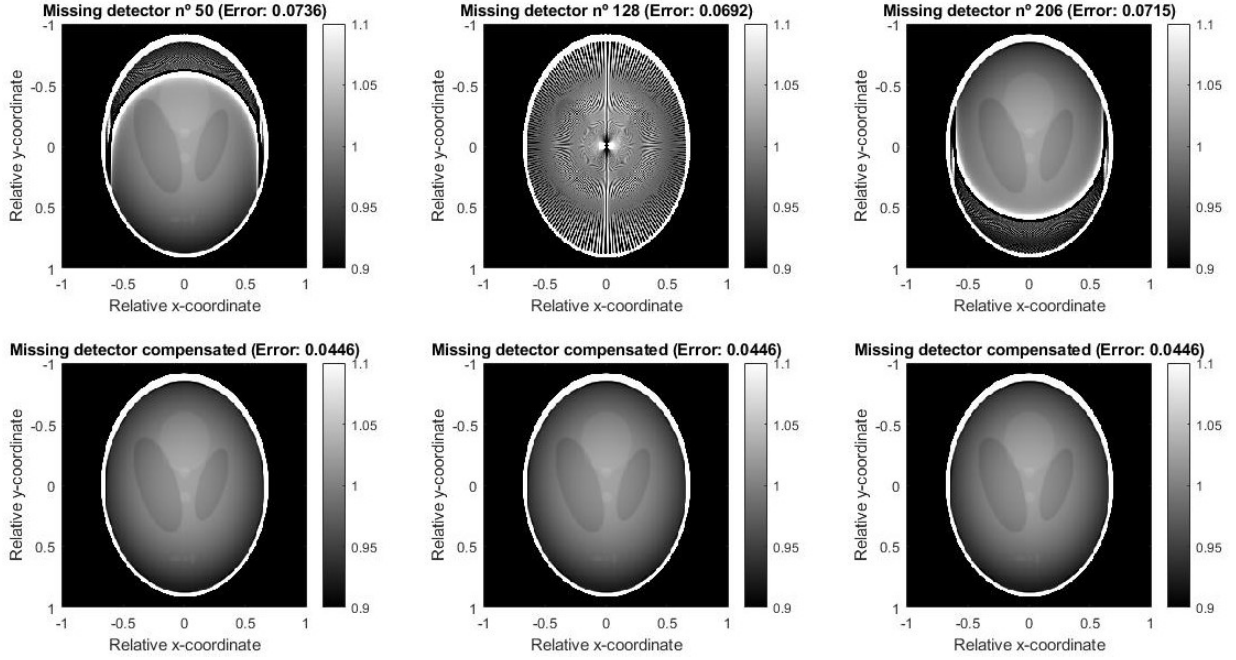


Figure 15: Effect of the missing detector number 50, 128 and 206 from left to right, respectively. (top) Reconstruction with a missing detector. (bottom) Reconstruction with the missing detector compensated.

To conclude this section, it is analysed the influence of all the possible positions of missing detectors with an error plot (see figure 16). The highest errors are found in the central positions since they have continuous direct influence in the phantom reconstruction (inside the white contour). In contrast, as long as the missing detector is getting closer to the extremes of the array of detectors, the error starts decreasing considerably. When the missing detector is located in the edges of the array, the error remains low and constant, due to the fact that the detectors located in the extremes have almost no influence in the final reconstruction, and most of the errors generated by them are removed by the mask (thus, no considered in the analysis). This, leads to the conclusion that a detector failing in the extremes may not be a major problem for the system if the width of the array is bigger than the width of the structure under reconstruction.

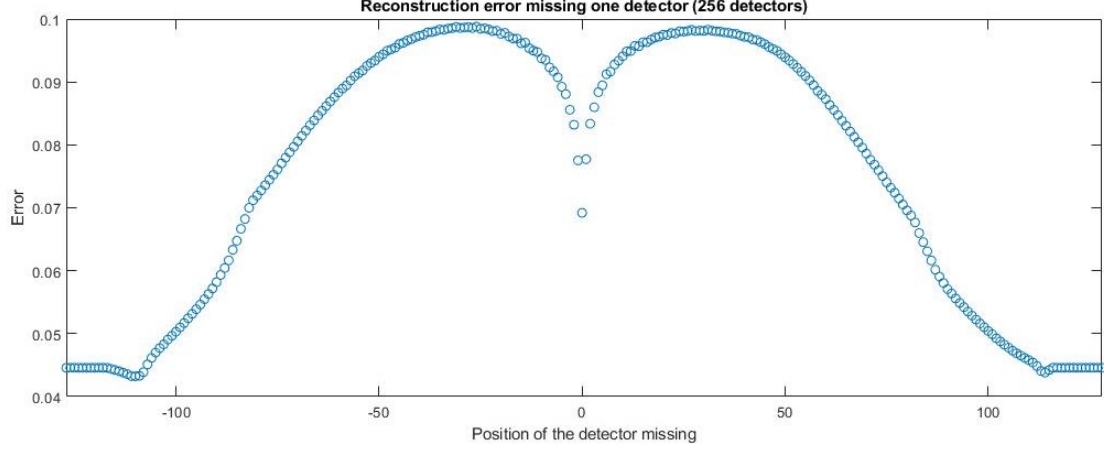


Figure 16: Error trend while sliding the missing detector over the array of 256 detectors.

4 In-vivo data

After that the implemented method was tested and verified in the simulation, it is used to reconstruct a clinical image with size 512 x 512 pixels. The data was obtained from a female patient by a Toshiba scanner at Rigshospitalet using 200 projections (parallel beams) over 180°.

4.1 Reconstruction analysis

In this section the system is applied to the in-vivo data. In figure 17 it is shown the obtained reconstructed image (center) in comparison with the corresponding frame obtained from the movie (left). As shown, the reconstructed image and the image (frame number 617) recover the same body structures and distributions, and setting to a certain saturation range, they get to look similar. Moreover, in figure 17 (right) there are highlighted the main anatomical structures of the pelvis. It can be noticed how the reconstructed image is able to distinguish the different structures: for instance, bones such as ilium and spinal cord (light green circle) are displayed. Ascending (dark green circle) and descending colon (red circle) can also be recognized. Lastly, the iliac arteries can be distinguished. In particular, right and left external iliac arteries are shown in orange and yellow circles, respectively, whereas right and left internal iliac arteries are shown in light blue and pink circles, respectively.

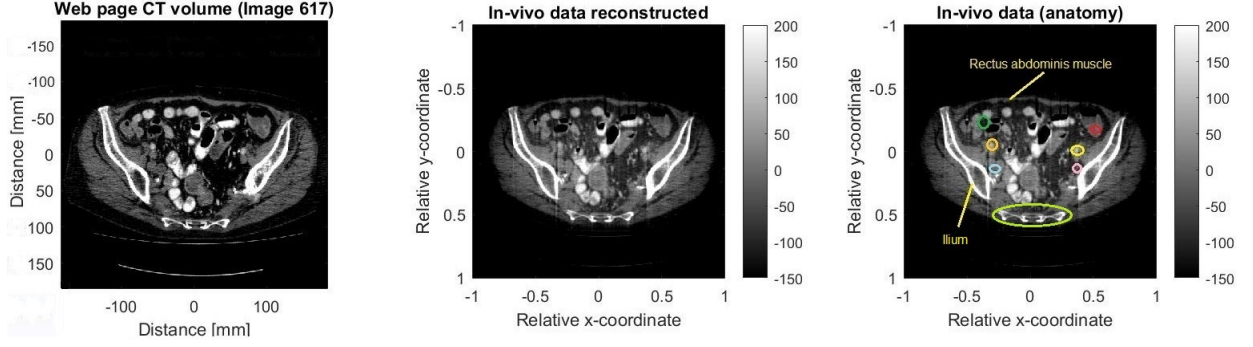


Figure 17: (left) Frame number 617 from the CT volume. (center) Reconstructed image from the in-vivo data with the developed system. (right) Reconstructed image highlighting the main structures.

One of the advantages of this system is that the reconstructed information can be easily saturated in order to differentiate tissues within the image. In figure 18 it is shown the reconstructed image saturated with different range of Hounsfield units in order to see different structures of the pelvis. On the left the compact bones are displayed using a range between 200 and 800 HU, therefore showing the ilium and spinal cord. On the center the spongy bones are showed using a range between 50 and 200 HU. Lastly, in the right image fat is highlighted by using a range between -100 and -80 HU, locating most of the fat in the edges of the body.

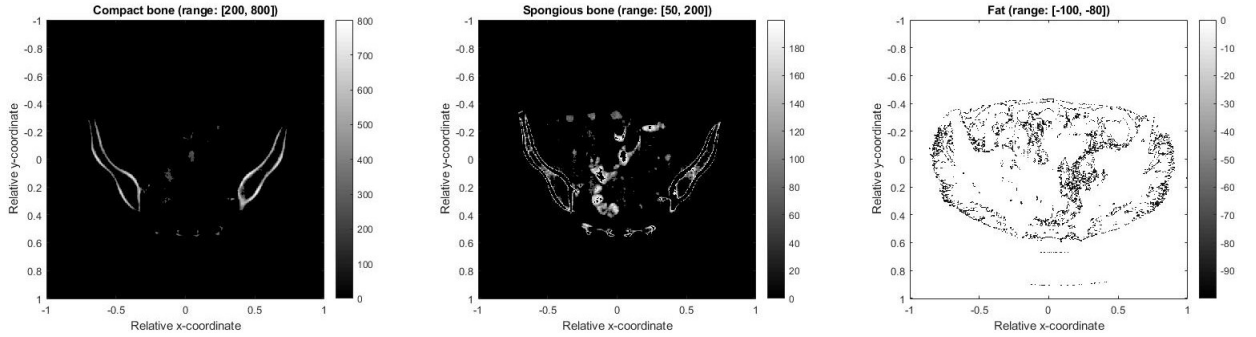


Figure 18: Saturation of the reconstructed image. (left) Compact bone. (center) Spongy bone. (right) Fat.

4.2 Effect of a missing detector

To conclude the results, it is decided to test what is the effect of a broken detector in a real image. In this case, the missing detector is located in the position 200 of the array (out of 512 detectors), and the result obtained is shown in figure 19 (left). There is a clear disturbance in the reconstructed image, although the main structures can still be distinguished.

Figure 19 (center) shows the result after compensating the missing detector. Despite the reconstructed image after compensating the detector looks like the original image obtained (see figure 17, center), if a subtraction between both of them is applied, it can be appreciated that the compensation is not perfectly working (see figure 19, right). In fact, there is an error difference of 0.3657 between the two images, although the purposed solution gives positive visual results.

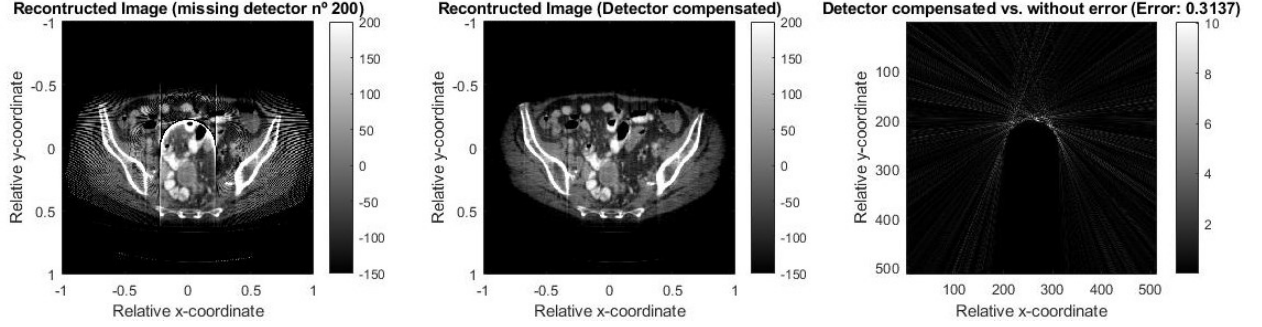


Figure 19: Missing detector images. (left) In-vivo reconstruction with missing detector in the position 200. (center) In-vivo reconstruction with missing detector compensated. (right) In-vivo reconstruction compensated vs. original reconstructed image (figure 17, center)

5 Conclusion

In general, the operation of the entire system returns positive results both visually, which shows a great similarity between the ideal Shepp-Logan phantom and the reconstructed ones, and in terms of error, giving values below 0.05.

Focusing more on the detail, in the case of study the selection of the filter has not returned critical values for any of the filters considered, so it can be concluded that they all have similar performances, providing the system with similar gain ranges and returning low error values in all cases (being the best Hann weighted filter).

On the other hand, regarding the variable parameters of the system, they are critical in order to reach a minimum resolution, but once reached certain values (i.e. 64 projections and 256 pixels) good reconstructions are achieved, so it is not necessary to continue increasing the value of the parameters (this will also help to obtain higher computing speeds for the reconstruction).

In fact, a velocity test of reconstruction was run in order to obtain more information about the performance of the software. It was used a computer (model ASUS ZenBook UX310) with the following specs: CPU (Intel Core i7-6500U) and RAM (8GB DDR3) during simulation and in-vivo data reconstruction. The time that it took to reconstruct the Shepp-Logan image (dimensions 100 projections and 256 pixels) and the clinical image

(dimensions 200 projections and 512 pixels) was 0.102574 s and 0.69986 s, respectively. The time difference between the two reconstructions is due to the different dimensions in the input data. In fact, looking through the code it is easy to allocate where this time difference is generated, so it can be concluded that the loop that runs the inverse Radon transform (see Appendices, *Listing 3: calculateInverseRadon.m.*, code lines: 23 to 28) is the critical part of the software in terms of computation time.

As regards when a detector is failing, the impact that it generates on the reconstruction of the final image is clear, although depending on the location of the messing detector, the image will be reconstructed in a better or worse way. In any case, the proposed solution of digitally interpolating this detector, facilitates the reconstruction of the image, giving the result very similar to those expected.

To conclude, the results obtained from the in-vivo data are clear, which facilitates the task of distinguishing the different structures of this cross section of the human body. Moreover, CT reconstruction has the advantage to be able to saturate the images in such a way that different groups of tissues can be completely differentiated.

References

- [1] J. L. Prince and J. M. Links, *Medical imaging signals and systems*. Pearson Prentice Hall Upper Saddle River, 2006.
- [2] A. P. Dhawan, *Medical image analysis*. John Wiley & Sons, 2011, vol. 31.
- [3] L. A. Shepp and B. F. Logan, “The fourier reconstruction of a head section,” *IEEE Transactions on nuclear science*, vol. 21, no. 3, pp. 21–43, 1974.